



# Effect of Mo on acicular ferrite transformation and interphase precipitation of Nb–V–N microalloyed steel during a continuous cooling process

Jing Zhang<sup>1</sup> · Wen-bin Xin<sup>1</sup> · Deng-yun Hou<sup>1</sup> · Jun Peng<sup>1</sup> · Zhi-bo Zhao<sup>2</sup> · Yang Tong<sup>1</sup>

Received: 13 March 2024 / Revised: 23 April 2024 / Accepted: 26 April 2024  
© China Iron and Steel Research Institute Group Co., Ltd. 2024

## Abstract

The substantial influences of Mo contents varying from 0 to 0.26 and 0.50 wt.% on the microstructural evolution and MX (M=Nb, V and Mo; X=C and N) precipitation characteristics of Nb–V–N microalloyed steels processed by hot deformation and continuous cooling were studied using a Gleeble 3800 thermomechanical simulator. Metallographic analysis showed that the ferrite microstructure transformed from polygonal ferrite (PF) in 0Mo steel to both acicular ferrite (AF) and PF in 0.26Mo and 0.50Mo steels, and AF content first increased and then decreased. The thermodynamic calculations and the experimental results proved that the quantity of solid solution of Mo in austenite obviously increased, which reduced the austenite ( $\gamma$ ) to ferrite ( $\alpha$ ) transformation temperature, consequently promoting AF formation in 0.26Mo steel and bainite transformation in 0.50Mo steel. Moreover, the submicron Nb-rich MX particles that precipitated at the temperature of the austenite region further induced AF heterogeneous nucleation with an orientation relationship of  $(011)_{MX} // (100)_{\text{Ferrite}}$  and  $[1\bar{1}1]_{MX} // [001]_{\text{Ferrite}}$ . The interphase precipitation of the nanosized V-rich MX particles with Mo partitioning that precipitated during  $\gamma \rightarrow \alpha$  transformation exhibited a Baker–Nutting orientation relationship of  $(100)_{MX} // (100)_{\text{Ferrite}}$  and  $[001]_{MX} // [01\bar{1}]_{\text{Ferrite}}$  with respect to the ferrite matrix. With increasing Mo content from 0 to 0.26 and 0.50 wt.%, the sheet spacing decreased from 46.9–49.0 to 34.6–38.6 and 25.7–28.0 nm, respectively, which evidently hindered dislocation movement and greatly enhanced precipitation strengthening. Furthermore, facilitating AF formation and interphase precipitation was beneficial to improving steel properties, and the optimal Mo content was 0.26 wt.%.

**Keywords** Nb–V–Mo–N microalloyed steel · Mo content · Acicular ferrite · Interphase precipitation · Secondary ion mass spectrometry

## 1 Introduction

As essential substances for infrastructure construction, structural steels are widely used in high-rise civil architecture [1, 2], large-scale offshore platforms [3, 4] and long-distance energy transportation systems [5, 6]. Elevating the fundamental strength and toughness is a promising measure

for decreasing the amount used in an application and for consequently satisfying the environmental requirements achieving carbon peak and carbon neutrality [7–9]. Moreover, microalloying technology involving the addition of Nb, V, Ti, Mo, etc., to low-carbon steels which exerts multiple synergistic positive effects on microstructures and precipitates has been commonly applied with a thermomechanical controlled process to improve steel properties [10–15].

It is acknowledged that grain refinement strengthening by the formation of intragranular ferrite (IGF) is an indispensable approach for simultaneously enhancing the strength and toughness parameters of microalloyed steels [16–19]. IGF can be classified as intragranular polygonal ferrite (IPF) composed of equiaxed grains and acicular ferrite (AF) composed of interlocked ferrite plates with

✉ Wen-bin Xin  
xwb2580zxc@163.com

<sup>1</sup> School of Rare Earth Industry (School of Rare Earth Engineering and Technology), Inner Mongolia University of Science and Technology, Baotou 014010, Inner Mongolia, China

<sup>2</sup> School of Materials and Metallurgy, Inner Mongolia University of Science and Technology, Baotou 014010, Inner Mongolia, China

distributed high-density dislocations [20, 21]. Compared to the improvement in steel properties by IPF, the advantages of acicular ferrite include the following aspects: (1) AF divides prior austenite grains into much smaller regions than before, contributing to a greater increase in grain refinement strengthening [22, 23]; (2) AF restrains crack initiation by releasing stress and arrests crack propagation by constructing high-angle grain boundaries with neighboring microconstituents [24, 25]; and (3) AF hardens the microstructure due to the intense interactions between nanoprecipitates and dislocations [26, 27]. Thus, acicular ferrite tends to be a candidate microstructure for obtaining good combinations of strength and toughness for microalloyed steels.

Several studies have reported that IPF and AF preferentially nucleate on second-phase particles, such as V(C, N) [28], (Ti, V)(C, N) [16] and (Nb, V)(C, N) [29], which precipitate in base materials and weld metals. As the phase transformation of polygonal ferrite (PF) competes with that of acicular ferrite, the solid solution of alloying elements in austenite and the application of cooling procedures that are beneficial to AF formation need to be considered, in addition to heterogeneous nucleation [19, 30, 31]. Mo in the solid solution state can suppress the decomposition of supercooled austenite and retard the transformation from austenite ( $\gamma$ ) to ferrite ( $\alpha$ ), facilitating the formation of the low-temperature microstructures [32–35]. Kong et al. [36] investigated the influences of Mo on the microstructure and mechanical properties of X80 pipeline steel and reported that the increase in AF proportion is accompanied by a decrease in the polygonal ferrite, and bainite and martensite/austenite (M/A) could be observed with the increase in Mo content from 0 to 0.41 wt.%. The microstructural changes in low-carbon pipeline steels with different Mo additions were studied, and continuous cooling transformation (CCT) diagrams indicated that Mo inhibits PF transformation and promotes AF formation [37]. However, Mo addition also leads to bainite and martensite transformation, as indicated by Hu et al. [38] and Shi et al. [39]. Moreover, AF transformation is largely dependent on the cooling rate during the continuous cooling process, which influences the austenite transformation kinetics. High cooling rates accelerate the formation of acicular ferrite and bainite but restrain the transformation of polygonal ferrite and pearlite [40–42]. Apparently, the effect of the bulk Mo content on microstructure transformation has been extensively studied, whereas the variation in the solid solute Mo in austenite with the addition of Mo, which is more directly related to phase transformation, has seldom been explored. In addition, the effect of this addition on AF formation, particularly in Nb–V–Mo–N quaternary microalloyed steels, is unknown.

Precipitation strengthening has been commonly applied to substantially increase the strength of the ferrite phase in microalloyed steels [8, 9, 43]. The carbonitride particles precipitated in the ferrite matrix are distributed randomly and/or in regularly parallel rows and classified as either random precipitation (RP) or interphase precipitation (IP). Moreover, the contribution of IP to the yield strength can reach 150–450 MPa without an observable loss of ductility, which is greater than that of RP [8, 44, 45]. This difference arises because the high number density and the presence of extremely fine nanoprecipitates (<10 nm) severely hinder dislocation movement during plastic deformation [46]. Funakawa et al. [47] developed a 780 MPa Ti–Mo ferritic steel with excellent formability using interphase precipitation strengthening. Later, a novel 1200 MPa grade NANOHTEN steel with a single ferrite matrix was developed by JFE [48]. Wang et al. [49] studied Ti–Mo dual-phase steel and reported that the ferritic microstructure strengthened by (Ti, Mo)C interphase precipitates is harder than bainite.

In fact, interphase precipitation occurs when carbonitrides periodically nucleate on migrating  $\gamma/\alpha$  interfaces during  $\gamma \rightarrow \alpha$  transformation, and the increase in IP strengthening depends on the volume fraction of the precipitated particles [43, 46, 50]. A decrease in the sheet spacing generally produces increases in the volume fraction and strength contribution, which are directly related to the addition of alloying elements; moreover, this change affects the characteristics of  $\gamma \rightarrow \alpha$  transformation and carbonitride precipitation [51]. Mo is a favorable element for the interphase precipitation of nanosized particles. Gong et al. [52] studied the effects of Mo on the interphase precipitation of isothermally treated Ti- and V-microalloyed steels and reported that the addition of Mo significantly decreases  $\gamma \rightarrow \alpha$  transformation kinetics, particularly in V steel, and produces a relatively great volume fraction of precipitates by reducing the misfit of the precipitates/matrix interface and the interfacial energy. Dong et al. [11] studied the significance of Mo on Ti steel with isothermal treatment and revealed that the number density of interphase precipitates increases with a small addition of 0.1 wt.% Mo, whereas it does not increase obviously with greater additions of Mo. Kamikawa et al. [53] investigated interphase precipitation characteristics of Ti and Ti–Mo steels and reported that Mo partitions into the TiC crystal lattice to form  $(\text{Ti}_{1-x}\text{Mo}_x)\text{C}$ , resulting in an increase in the number density. Jang et al. [54] proved that Mo can partially replace Ti atoms in TiC carbides, reducing the interfacial energy and the nucleation driving force, based on first-principles calculation. Although the influence of the bulk Mo content on interphase precipitation has been substantially studied in isothermally treated Ti steel, further investigations are needed to determine the influence of the bulk Mo content on

interphase precipitation in Nb–V–Mo–N composite microalloyed steels processed by continuous cooling and hot deformation with greater industrial relevance.

In the present work, Nb–V–N microalloyed steels containing a series of Mo contents were designed to clarify the effect of Mo. In detail, Mo solid dissolved in austenite instead of the bulk Mo addition has been qualitatively and quantitatively investigated, and the dynamic CCT curves were constructed to understand the influence of Mo on acicular ferrite formation. Moreover, the intrinsic physical characteristics of the interphase precipitates, including the driving force and interfacial energy in ( $\gamma+\alpha$ ) temperature range, which vary with Mo content, were analyzed to elucidate the significance of Mo for interphase precipitation and were simultaneously found to be correlated with the external continuous cooling transformation.

## 2 Experimental

### 2.1 Materials and thermomechanical controlled processes

Three 25-kg Nb–V–N microalloyed steel ingots with Mo contents varying from 0 to 0.26 and 0.50 wt.%, denoted as 0Mo, 0.26Mo and 0.50Mo, respectively, were melted in a vacuum induction furnace. Table 1 presents the chemical compositions of the experimental steels. The ingots were heated in 1250 °C for 2 h, hot-forged into bars with a diameter of 18 mm in a temperature range of 950–1150 °C and finally air-cooled to ambient temperature. The steel bars were first annealed at 900 °C for 1 h, furnace-cooled to ambient temperature and then cut into specimens for thermomechanical simulation.

A continuous cooling process with different cooling rates after hot deformation was conducted on a Gleeble 3800 thermomechanical simulator, simultaneously obtaining the corresponding dilation–temperature–time data for plotting the dynamic CCT curves. As shown in Fig. 1, the specimens were first heated to 1200 °C for 300 s, subjected to strain compression of 0.4 at a recrystallization temperature of 1050 °C and strain compression of 0.3 at a nonrecrystallization temperature of 900 °C, and finally cooled to

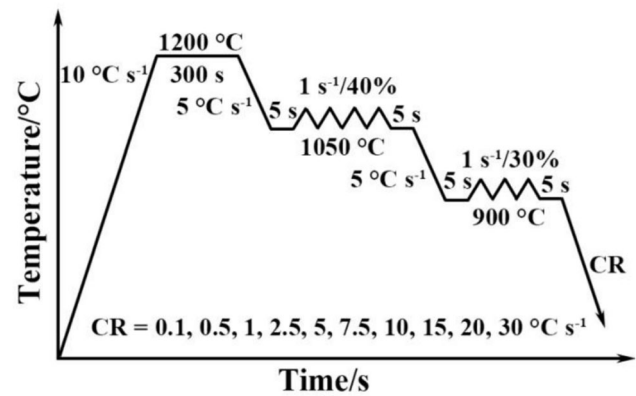


Fig. 1 Schematic illustration of thermomechanical simulation tests

ambient temperature at cooling rates (CRs) ranging from 0.1 to 30 °C/s. In addition, to analyze the amount of dissolved Mo in austenite, the water-quenched specimens with a dimension of 10 mm×10 mm×5 mm were first cut at the center of as-annealed steel bars along the longitudinal axis, then heated at 1200 °C for 300 s and immediately cooled to ambient temperature by water quenching.

### 2.2 Thermodynamic calculation

Under equilibrium condition, the precipitation thermodynamics of MX (M=Nb, V and Mo; X=C and N) phases, including the driving force and interfacial energy, and the solid solution characteristics of Mo atoms in austenite were calculated based on Thermo-Calc software and the TCFE 12 database. Moreover, the characteristic temperatures of  $A_{e1}$  and  $A_{e3}$  were also calculated and are listed in Table 1 which were applied to set the austenite temperature region and the (austenite+ferrite) two-phase temperature region for the above-mentioned calculation.

### 2.3 Microstructural characterization

To investigate the microstructural characteristics and MX precipitation behavior, metallographic samples were first transversally sectioned at thermocouple solder joint of thermomechanical simulated specimens and then ground, polished and etched with 4 vol.% Nital for observation via

Table 1 Chemical compositions and characteristic temperatures of Nb–V–Mo–N experimental steels

Sample	Element content/wt.%									Temperature/°C	
	C	Si	Mn	P	S	Nb	V	Mo	N	$A_{e1}$	$A_{e3}$
0Mo	0.17	0.35	1.52	0.005	0.004	0.100	0.22	–	0.014	690	820
0.26Mo	0.17	0.36	1.54	0.003	0.004	0.098	0.21	0.26	0.017	690	830
0.50Mo	0.17	0.37	1.54	0.003	0.004	0.100	0.21	0.50	0.015	690	830

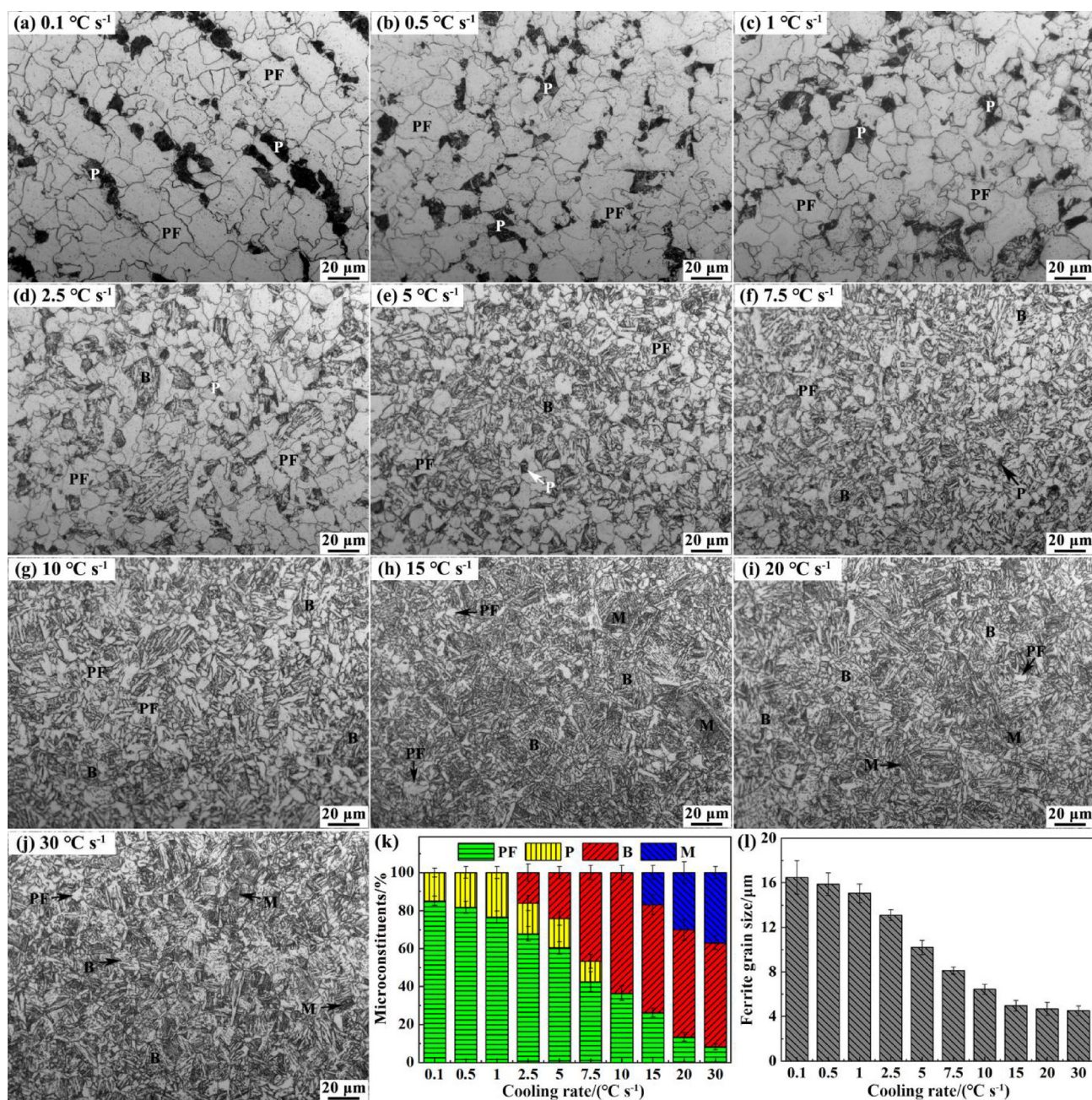


Fig. 2 OM micrographs (a–j), microconstituents (k) and ferrite grain sizes (l) of 0Mo steel cooled at different cooling rates

optical microscopy (OM, Zeiss Axio Vert.A1), field emission scanning electron microscopy (FE-SEM, Zeiss Sigma 300) and energy-dispersive spectroscopy (EDS, Oxford). Transmission electron microscopy (TEM, FEI Tecnai G2 F30) in conjunction with energy-dispersive X-ray spectrometry (EDAX, Ametek) was carried out on thin-film specimens prepared by ion milling. Electron probe microanalysis (EPMA, JXA-iHP200F) was performed on water-quenched specimens. In addition, the microconstituents

(i.e., area fraction of each microstructure), ferrite grain size and precipitated particle size were measured by Image-Pro Plus software.

Time-of-flight secondary ion mass spectrometry (ToF-SIMS, ION-TOF GmbH) was conducted on the water-quenched specimens, which were analyzed using a Bi<sub>1</sub><sup>+</sup> primary sputtering ion beam at 30 keV and an O<sub>2</sub><sup>+</sup> secondary ion gun in positive mode at 2 keV. The scanning area was 200 μm × 200 μm, and the total time was approximately 60 min.

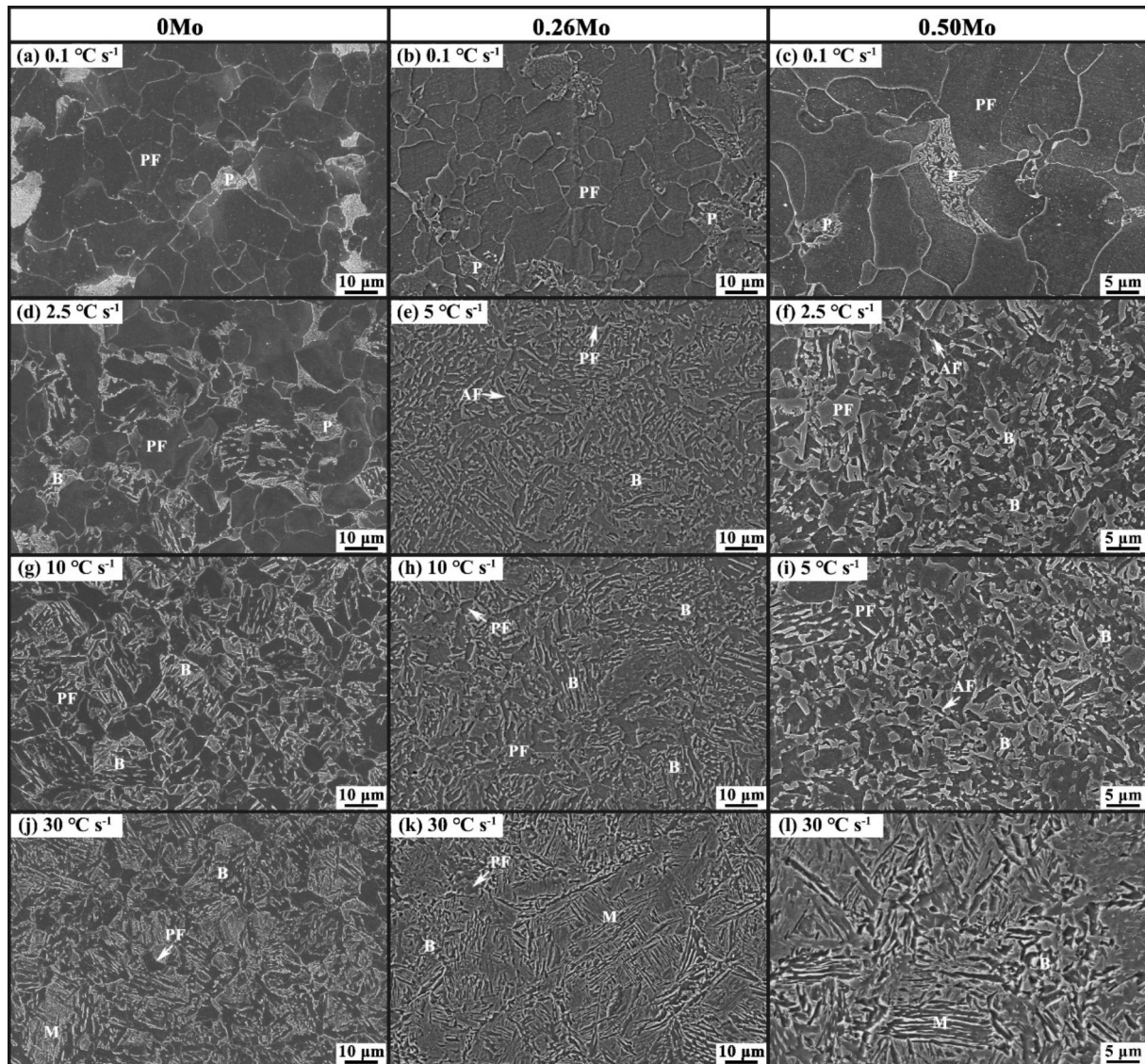


Fig. 3 SEM micrographs of 0Mo, 0.26Mo and 0.50Mo steels cooled at different cooling rates

## 2.4 Microhardness

The microhardnesses of the metallographic specimens were measured at 10 randomly selected regions using a Qness Q10 A+ type Vickers hardness tester with a load of 0.98 N (0.1 kg) and a dwell time of 10 s. Moreover, the Vickers hardness measurement was also used to distinguish bainite from martensite in addition to morphology observation of microstructure. For the investigated steels, the Vickers hardness of bainite is mainly in the range of 250–300 HV0.1, while that of martensite is generally higher than 300 HV0.1.

## 3 Results

### 3.1 Microstructural characteristics

Representative OM and SEM images and the statistical microconstituents and ferrite grain sizes of 0Mo, 0.26Mo and 0.50Mo steels continuously cooled at different cooling rates after hot deformation are shown in Figs. 2–5. Figures 2a–c and 3a evidently show that the microstructure of 0Mo steel at 0.1, 0.5 and 1 °C/s was predominantly composed of PF and some pearlite (P) colonies. With an increase in the cooling rate to 2.5 °C/s, the supercooled

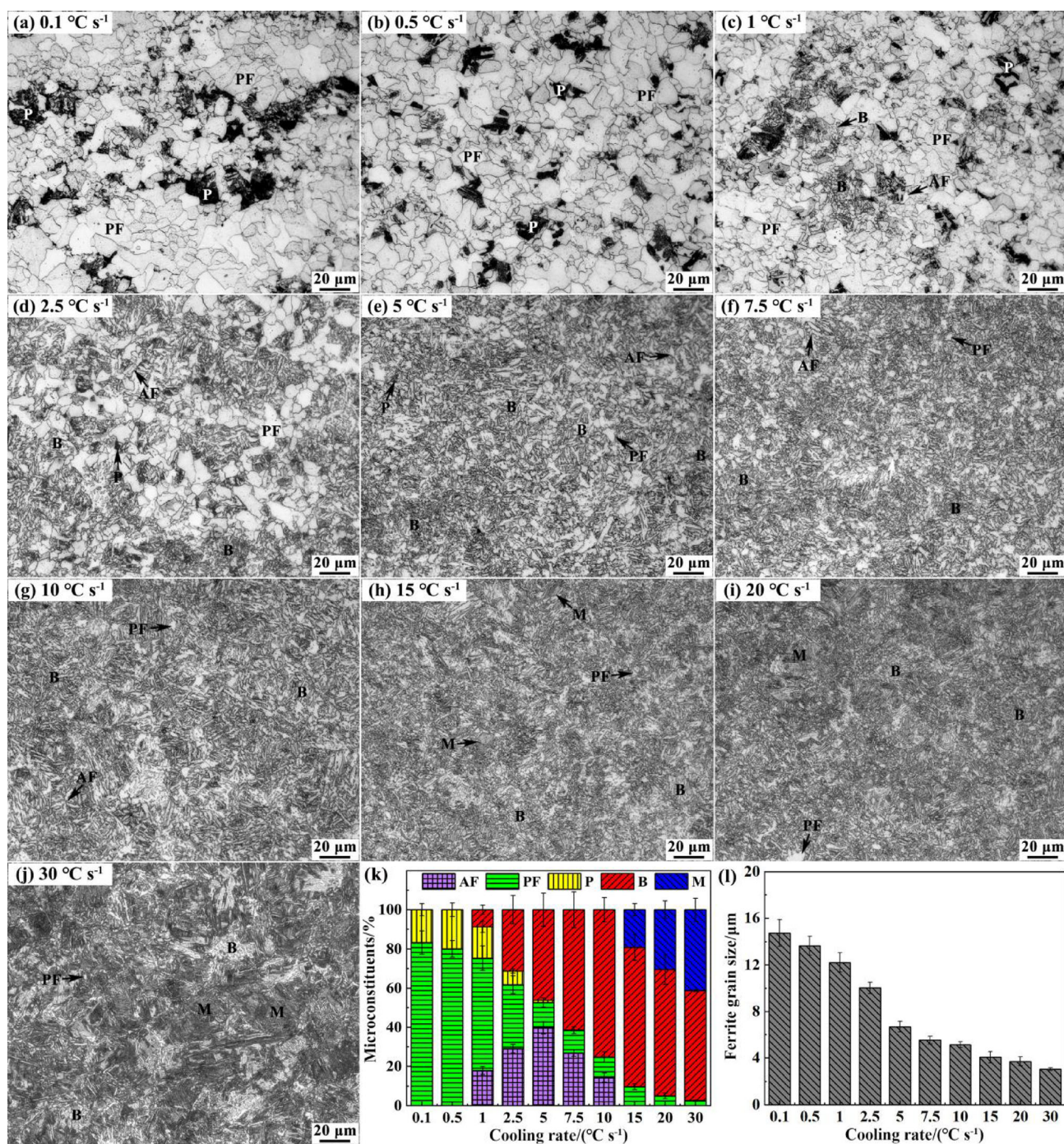


Fig. 4 OM micrographs (a–j), microconstituents (k) and ferrite grain sizes (l) of 0.26Mo steel cooled at different cooling rates

austenite transformed into bainite (B) apart from PF and P, as shown in Figs. 2d and 3d. Figures 2e–g and 3g show that the area fraction of bainite increased and those of ferrite and pearlite obviously decreased. At 10 °C/s, the pearlite disappeared, and the ferrite grains were mainly distributed at the prior austenite grain boundaries. Figure 2h shows that martensite (M) appeared at 15 °C/s. When the cooling rate further increased to 30 °C/s, the area fraction of martensite

increased, accompanied by a decrease in ferrite and bainite, as shown in Figs. 2i, j and 3j. Figure 2k shows that the area fraction of polygonal ferrite decreased from  $85.1\% \pm 2.35\%$  to  $8.3\% \pm 1.54\%$  when the cooling rate increased from 0.1 to 30 °C/s. For pearlite, the area fraction first increased from  $14.9\% \pm 2.35\%$  to  $23.4\% \pm 3.13\%$  at 0.1–1 °C/s and then decreased progressively due to bainite transformation until it disappeared at 10 °C/s. Similarly, the area fraction of

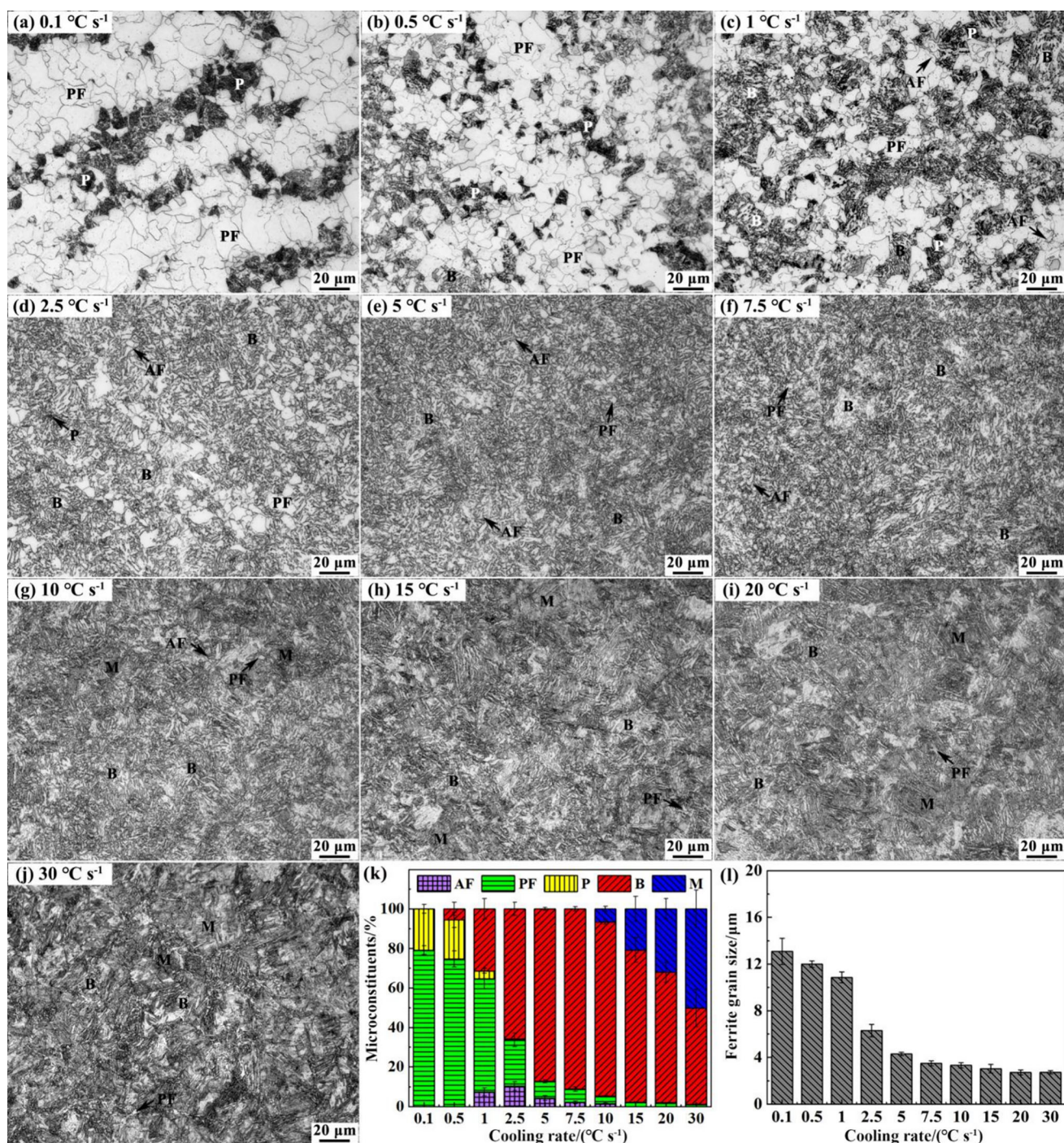
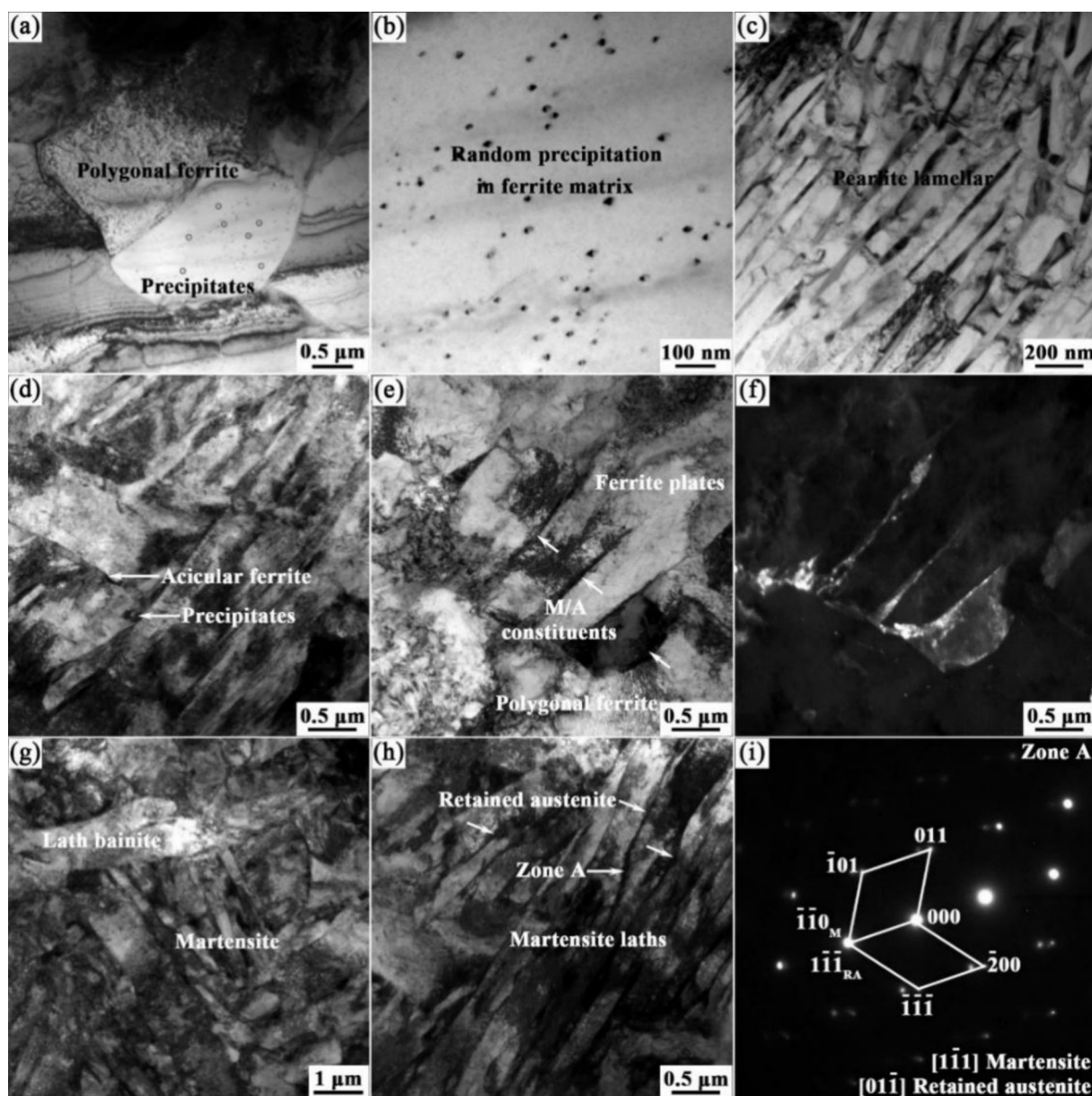


Fig. 5 OM micrographs (a–j), microconstituents (k) and ferrite grain sizes (l) of 0.50Mo steel cooled at different cooling rates

bainite first increased from  $16.0\% \pm 4.58\%$  to  $63.6\% \pm 3.83\%$  at 2.5–15 °C/s and then decreased to  $54.8\% \pm 3.60\%$  at 30 °C/s. The martensite content increased from  $16.9\% \pm 3.64\%$  to  $36.9\% \pm 3.20\%$  as the cooling rate increased from 15 to 30 °C/s. Moreover, the average ferrite grain size continuously decreased from  $16.5 \pm 1.51$  to  $4.5 \pm 0.43$  μm, as shown in Fig. 2l. The increased cooling rate increased the degree of supercooling, resulting in a relatively high nucleation

rate of ferrite, and restrained the diffusion of Fe and C atoms, which collectively suppressed ferrite grain growth.

Figures 3 and 4 show that the supercooled austenite of 0.26Mo steel transformed into polygonal ferrite, pearlite, bainite and martensite at cooling rates varying from 0.1 to 30 °C/s; these microstructural evolution characteristics were similar to those of 0Mo steel. In particular, the phase transformation of acicular ferrite occurred at 1–10 °C/s



**Fig. 6** TEM analyses of microstructures of 0.26Mo steel cooled at different cooling rates. **a–c**  $0.1\text{ }^{\circ}\text{C s}^{-1}$ ; **d–f**  $5\text{ }^{\circ}\text{C s}^{-1}$ ; **g**  $15\text{ }^{\circ}\text{C s}^{-1}$ ; **h, i**  $30\text{ }^{\circ}\text{C s}^{-1}$

when Mo content increased from 0 to 0.26 wt.%, as shown in Figs. 3e, h and 4c–g. The area fraction of AF first increased from  $17.8\% \pm 2.01\%$  to  $39.7\% \pm 3.17\%$  and then decreased to  $14.4\% \pm 2.32\%$  with increasing cooling rate, and the maximum value was obtained at  $5\text{ }^{\circ}\text{C/s}$ . Moreover, bainite transformation started to occur at  $1\text{ }^{\circ}\text{C/s}$ . By comparing the microstructural characteristics of 0.50Mo steel shown in Figs. 3 and 5 to those of 0Mo and 0.26Mo steels, it was apparent that the critical cooling rate of bainite transformation further decreased to  $0.5\text{ }^{\circ}\text{C/s}$ , and its area fraction basically increased at the same cooling rate. Acicular ferrite could be similarly observed at  $1\text{--}10\text{ }^{\circ}\text{C/s}$ , whereas most of AF with an area fraction of  $10.3\% \pm 2.24\%$

was acquired at  $2.5\text{ }^{\circ}\text{C/s}$ , which was lower than that of 0.26Mo steel. In addition, increasing Mo content contributed to ferrite grain refinement because of the solute drag effect from Mo in the solid solution state, as indicated by Yoo et al. [55], which was consistent with the results obtained for V–Mo [52] and Nb–Mo [55] microalloyed steels.

Figure 6 shows TEM analysis images of the microstructure of 0.26Mo steel cooled at different cooling rates. In Fig. 6a, ferrite grains with approximately equiaxed morphologies were observed at  $0.1\text{ }^{\circ}\text{C/s}$ , and the nanosized precipitates were randomly distributed in the ferrite matrix, as circled in red and correspondingly



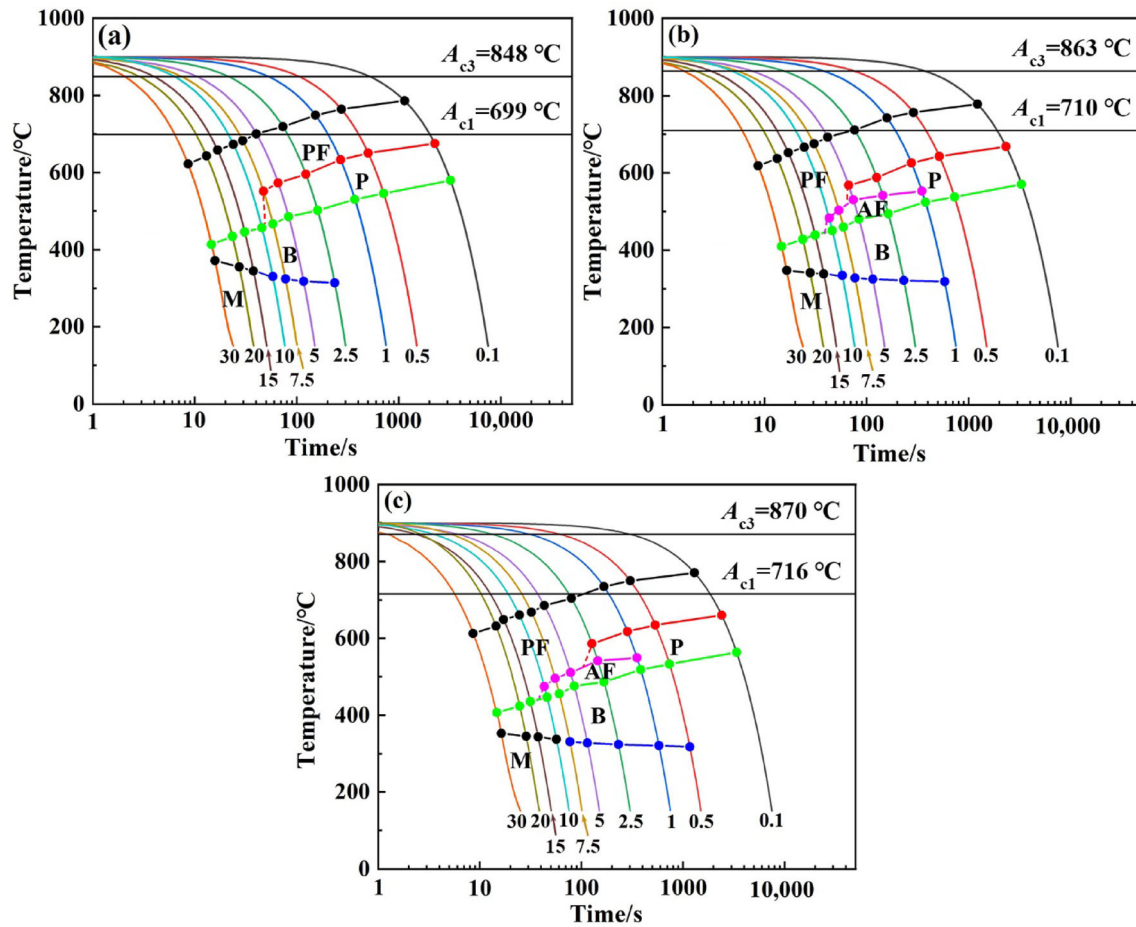


Fig. 7 Dynamic continuous cooling transformation curves of 0Mo (a), 0.26Mo (b) and 0.50Mo (c) steels

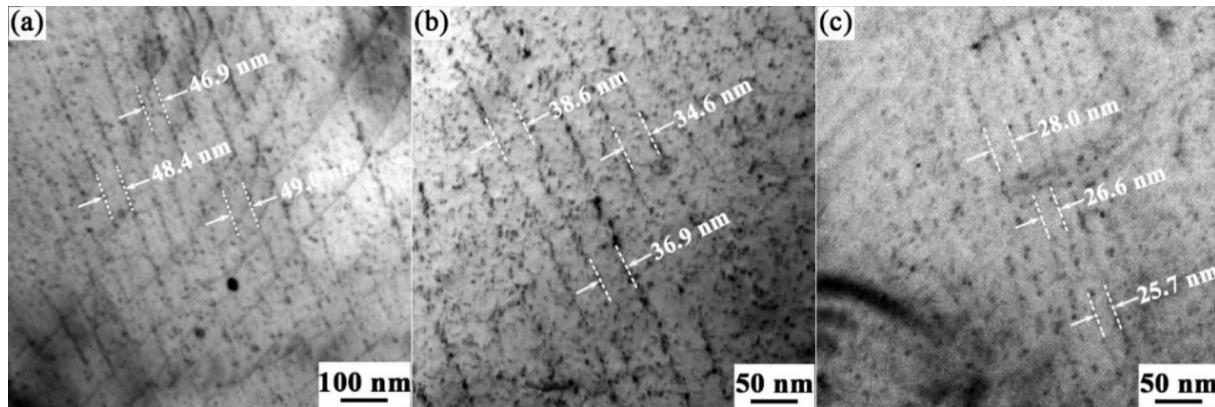


Fig. 8 Bright-field TEM images of interphase precipitation in 0Mo (a), 0.26Mo (b) and 0.50Mo (c) steels cooled at 1 °C s<sup>-1</sup>

magnified in Fig. 6b. Figure 6c shows the typical lamellar morphology of pearlite at 0.1 °C/s. The acicular ferrite obtained at 5 °C/s was characterized by interlocked non-quiaxed ferrite plates wrapped with high-density dislocations, as shown in Fig. 6d. Figure 6e and f shows bright-field image and dark-field image of the slender M/A constituents distributed between the ferrite plates obtained

at 5 °C/s. When the cooling rate reached 15 °C/s, the bainitic sheaves and martensite laths were observed, as shown in Fig. 6g. Figure 6h and i presents the parallel distributed laths of martensite and the strip-like retained austenite (RA) at 30 °C/s, following a variant of the Kurdjumov–Sachs (K–S) orientation relationship:  $(\bar{1}\bar{1}0)_M // (\bar{1}\bar{1}\bar{1})_{RA}$  and  $(1\bar{1}\bar{1})_M // (01\bar{1})_{RA}$ .

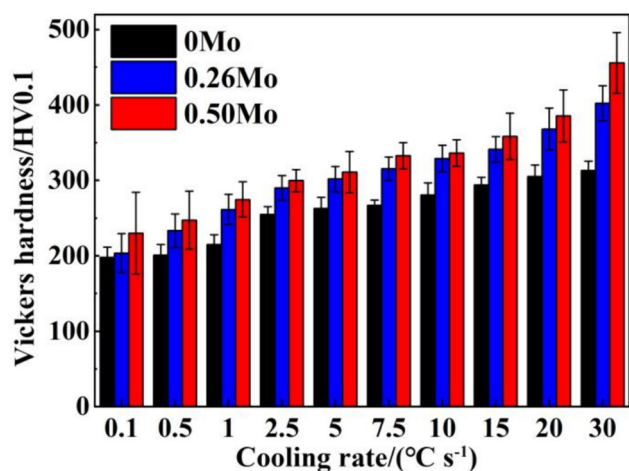


Fig. 9 Microhardnesses of experimental steels cooled at different cooling rates

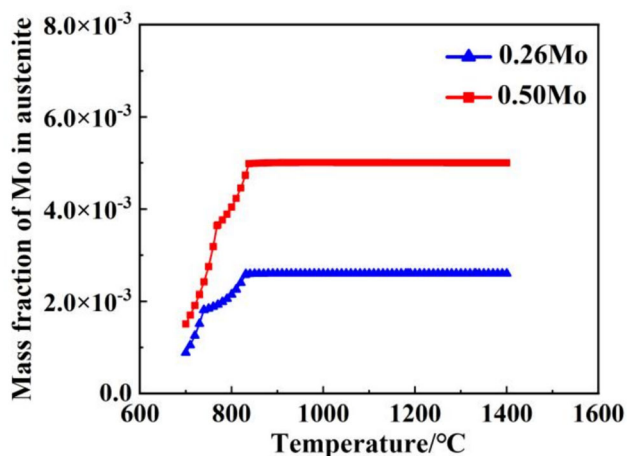


Fig. 10 Mass fractions of Mo in austenite phase of 0.26Mo and 0.50Mo steels as a function of temperature

### 3.2 Dynamic CCT curves

The dynamic CCT curves of 0Mo, 0.26Mo and 0.50Mo steels were plotted based on dilation–temperature–time data, microstructure observation and microhardness measurement, as shown in Fig. 7. Figure 7a shows that 0Mo steel was transformed into polygonal ferrite, pearlite, bainite and martensite at cooling rates of 0.1–30, 0.1–7.5, 2.5–30 and 15–30 °C/s, respectively. Correspondingly, the starting transformation temperatures of PF, P and B decreased from 786, 675 and 502 °C to 622, 551 and 414 °C, respectively, whereas that of M increased from 345 to 371 °C. When Mo content increased from 0 to 0.26 wt.%, the decomposition temperature of the supercooled austenite obviously decreased, and it transformed into acicular ferrite at 1–10 °C/s as the initial transformation temperature decreased from 553 to 483 °C, as shown in Fig. 7b. Moreover, the pearlite transformation interval evidently decreased as the

cooling rate decreased from 10 to 7.5 °C/s, whereas the bainite transformation interval broadened as the critical cooling rate decreased from 2.5 to 1 °C/s. In terms of 0.50Mo steel, the transformation of supercooled austenite was further postponed until a lower temperature was reached, and both AF and P transformation intervals decreased in contrast to the interval of B, as shown in Fig. 7c. In addition, the critical starting and finishing temperatures of ferrite to austenite, i.e.,  $A_{c1}$  and  $A_{c3}$ , increased from 699 and 848 °C to 710 and 863 °C and to 716 and 870 °C when Mo content increased from 0 to 0.26 and 0.50 wt.%, respectively.

### 3.3 Interphase precipitation

Figure 8 shows a typical TEM micrograph of interphase precipitation for 0Mo, 0.26Mo and 0.50Mo steels cooled at 1 °C/s. The interphase precipitates distributed in the ferrite matrix exhibited a regular row-like morphology when the thin film under TEM observation was tilted parallel to the planes in which the precipitates formed during  $\gamma \rightarrow \alpha$  transformation. Moreover, the sheet spacing of interphase precipitation decreased from 46.9–49.0 to 34.6–38.6 and 25.7–28.0 nm as Mo content increased from 0 to 0.26 and 0.50 wt.%, respectively. Notably, interphase precipitates were locally distributed in ferrite matrix of 0.50Mo steel, and they were not observed in the upper left region of Fig. 8c, resulting in a decreased volume fraction of nanosized particles.

### 3.4 Microhardness

The average microhardnesses of the experimental steels varied with respect to the cooling rate, as shown in Fig. 9. The values for 0Mo, 0.26Mo and 0.50Mo steels increased from  $198 \pm 13.5$ ,  $204 \pm 25.9$  and  $230 \pm 54.5$  HV0.1 to  $313 \pm 12.5$ ,  $402 \pm 23.2$  and  $456 \pm 40.2$  HV0.1, respectively, as the cooling rate increased from 0.1 to 30 °C/s, which was directly related to the refined microstructure, nanosized precipitates and hardened phases of bainite and martensite.

## 4 Discussion

### 4.1 Effect of Mo on AF transformation

As the solid dissolved Mo atoms in austenite affect its phase transformation, the qualitative and quantitative Mo distributions were comprehensively analyzed under both equilibrium and nonequilibrium conditions.

Figure 10 shows that the solid solution quantity of Mo in the austenite phase varied with temperature, and 0.26Mo steel had a variation trend similar to that of

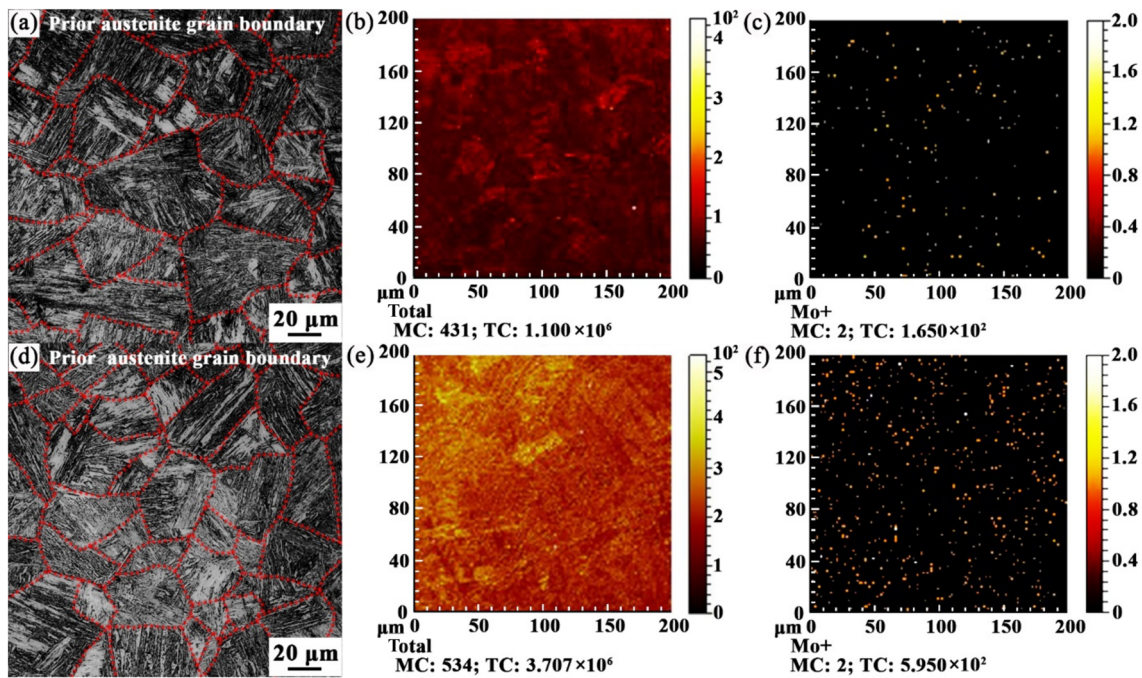


**Fig. 11** OM micrographs illustrating prior austenite grain boundaries and ToF-SIMS analyses of water-quenched specimens. **a–c** 0.26Mo steel; **d–f** 0.50Mo steel

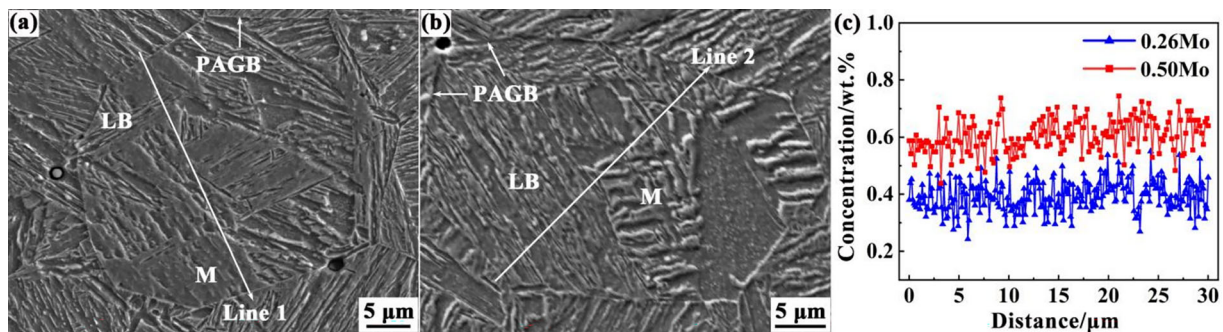


**Fig. 12** EPMA analyses of water-quenched specimens. **a** SEM micrograph of 0.26Mo steel; **b** SEM micrograph of 0.50Mo steel; **c** WDS line scanning of Mo steel

0.50Mo steel at the equilibrium state. When the temperature decreased from 1400 to 830 °C, the amounts of dissolved Mo atoms in 0.26Mo and 0.50Mo steels were basically unchanged and obviously decreased with decreasing temperature from 830 to 730 and 760 °C, probably due to the diffusion of Mo atoms into the ferrite phase. As the temperature further decreased, the amount of dissolved Mo decreased dramatically due to the precipitation of Mo-containing MX phase. Furthermore, the solid dissolved Mo in austenite was markedly elevated with increasing Mo addition to steel.

To address the question concerning solid dissolved Mo in the nonequilibrium state, ToF-SIMS characterization was conducted on water-quenched specimens of 0.26Mo and 0.50Mo steels, as shown in Fig. 11. Figure 11a and d shows

OM micrographs of the microstructure with the prior austenite grain boundaries marked by the red dotted lines. Figure 11b, c, e and f shows the intensities of the total detected ions and the individual Mo<sup>+</sup> ion clusters. The total counts of Mo<sup>+</sup> ions in 0.26Mo and 0.50Mo steels were  $1.650 \times 10^2$  and  $5.950 \times 10^2$ , respectively, and the increased Mo content increased the number of detected Mo<sup>+</sup> ions, particularly at the prior austenite grain boundaries. In addition, line scanning was conducted on an EPMA instrument equipped with a wavelength-dispersive spectroscopy (WPS) device, and the result was analyzed for a complete prior austenite grain, as shown in Fig. 12. By comparing the quantified Mo concentration of 0.26Mo steel to that of 0.50Mo steel, it was found that the average concentration increased with increasing bulk Mo content from

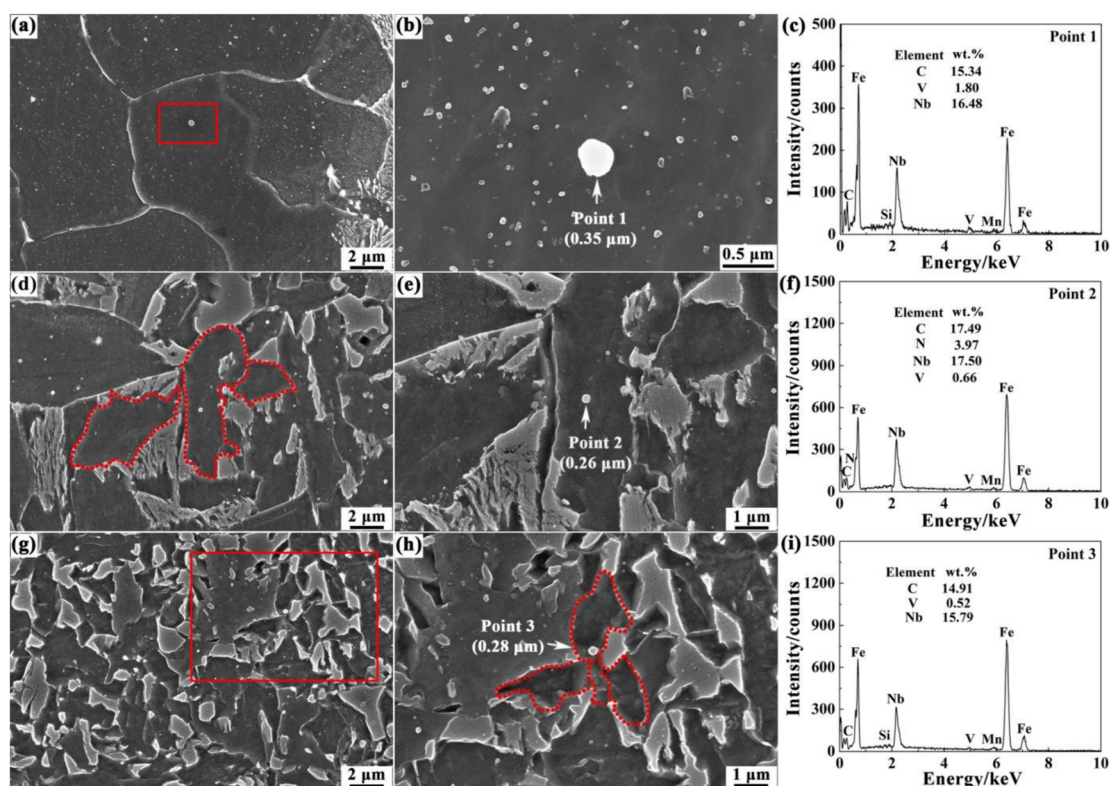


**Fig. 13** SEM micrograph and EDS spectrum of submicron particles precipitated in experimental steels cooled at different cooling rates. **a–c** 0Mo steel at  $0.1\text{ }^{\circ}\text{C s}^{-1}$ ; **d–f** 0.26Mo steel at  $2.5\text{ }^{\circ}\text{C s}^{-1}$ ; **g–i** 0.50Mo steel at  $5\text{ }^{\circ}\text{C s}^{-1}$

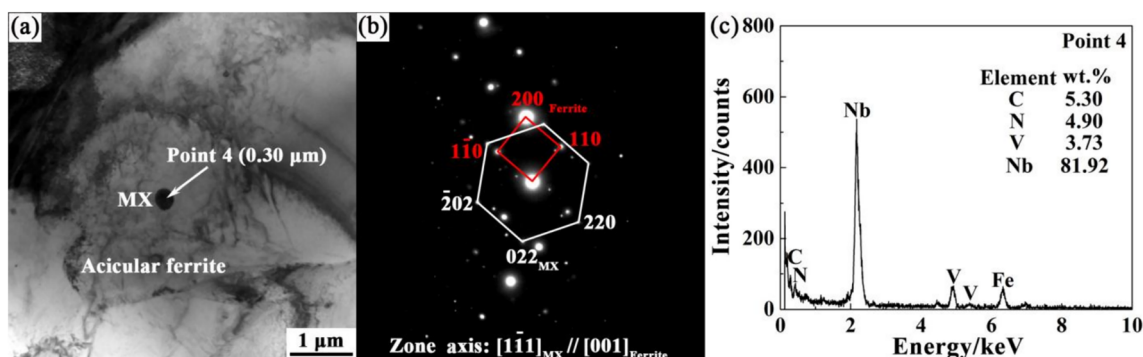


**Fig. 14** TEM analysis of submicron particle precipitated in 0.26Mo steel cooled at  $5\text{ }^{\circ}\text{C s}^{-1}$ . **a** Bright-field image; **b** SAED pattern; **c** EDS spectrum

0.393 to 0.606 wt.%. Notably, Mo concentrations fluctuated at the grain boundaries and at the bainite sheaves and martensite laths.

From the above-mentioned analysis, it was proved that the amount of solid dissolved Mo atoms obviously increased as the bulk Mo content increased from 0 to 0.26 and 0.50 wt.%; specially, a higher Mo content stabilized the supercooled austenite and reduced its decomposition temperature, which consequently accelerated the transformation of acicular ferrite in 0.26Mo steel and bainite in 0.50Mo

steel compared with the microstructural changes in 0Mo steel.

SEM micrographs and EDS spectra of the submicron microalloy carbonitrides in 0Mo, 0.26Mo and 0.50Mo steels precipitated in the austenite temperature region are shown in Fig. 13. The submicron-scale spherical Nb-rich MX particles (Points 1–3) played essential roles in the form of nucleation sites, stimulating the formation of PF in 0Mo steel and AF in 0.26Mo and 0.50Mo steels via heterogeneous nucleation. Furthermore, based on the selected area

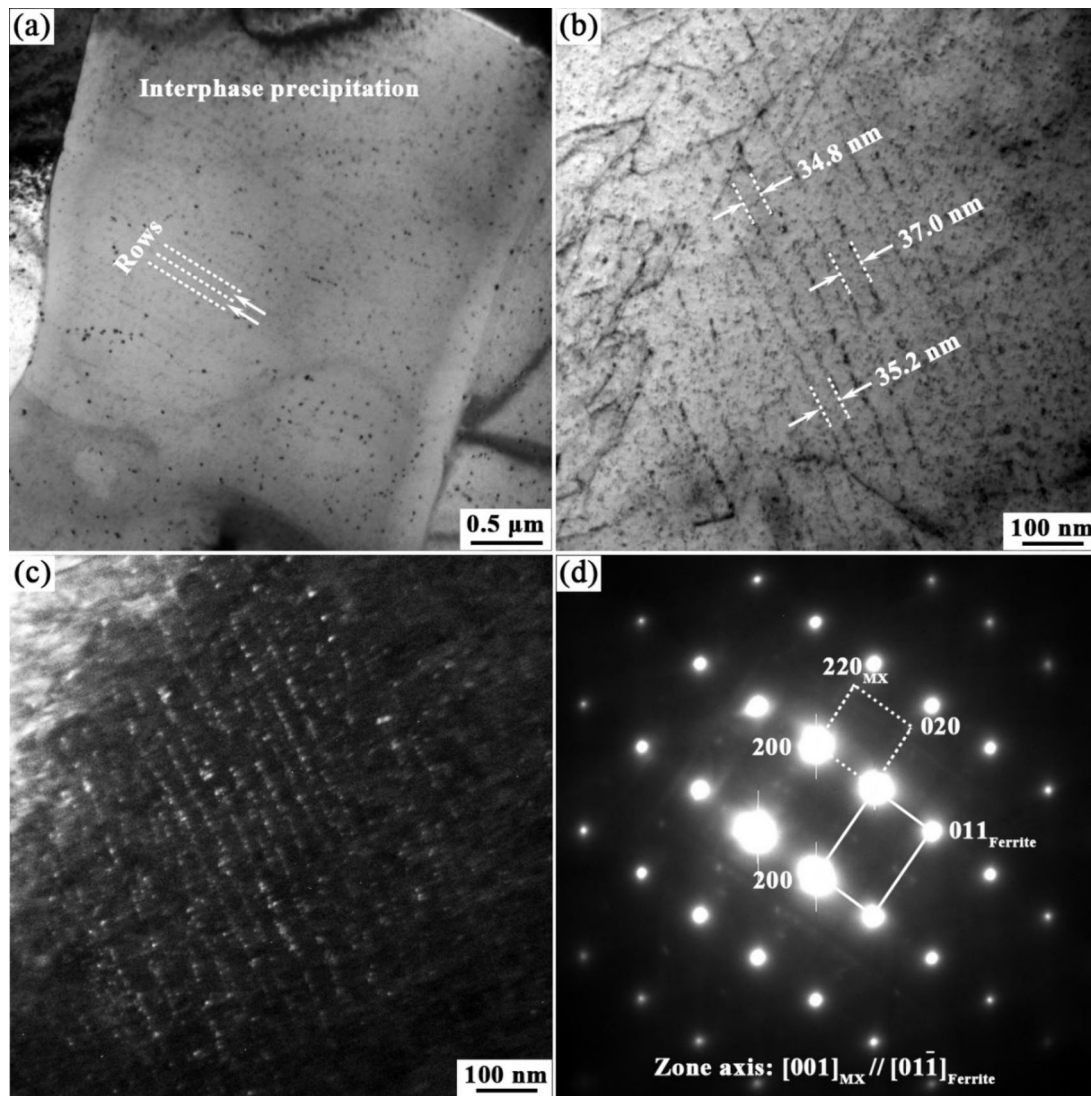


**Fig. 15** TEM analysis of interphase precipitation in 0.26Mo steel cooled at  $1\text{ }^{\circ}\text{C s}^{-1}$ . **a** Bright-field image at low magnification; **b** bright-field image at high magnification; **c** corresponding dark-field image; **d** SAED patterns

electron diffraction (SAED) patterns, the submicron-scale Nb-rich MX particle (Point 4) followed the orientation relationship  $(011)_{\text{MX}}// (100)_{\text{Ferrite}}$  and  $[1\bar{1}1]_{\text{MX}}// [001]_{\text{Ferrite}}$  with respect to the acicular ferrite, as shown in Fig. 14.

In summary, AF formation process was not only related to decreasing nucleation barrier of the Nb-rich MX particles but also dependent on the decrease in  $\gamma \rightarrow \alpha$  transformation temperature of the solid solution of Mo atoms; the optimal Mo addition to promote AF formation in Nb–V–N microalloyed steels was 0.26 wt.%.

#### 4.2 Effect of Mo on interphase precipitation

Interphase precipitation of nanosized particles was determined to be a potential method for strengthening the microstructure of ferrite and improving the performance of

microalloyed steels. Figure 15 shows bright-field and dark-field TEM images of the interphase precipitates in 0.26Mo steel continuously cooled at  $1\text{ }^{\circ}\text{C/s}$ , and the nanoprecipitates followed the Baker–Nutting (B–N) orientation relationship  $(100)_{\text{MX}}// (100)_{\text{Ferrite}}$  and  $[001]_{\text{MX}}// [00\bar{1}]_{\text{Ferrite}}$  with respect to the ferrite matrix. To demonstrate the compositions of the precipitates at the nanoscale, TEM micrographs, EDS spectra, high-angle annular dark field–scanning transmission electron microscopy (HAADF–STEM) images and corresponding STEM–EDS maps of Fe, Mo, V and Nb in 0.26Mo steel cooled at  $0.1\text{ }^{\circ}\text{C/s}$  are shown in Fig. 16. The nanosized particles were V-rich MX precipitates; specially, Mo atoms were partitioned into V-containing carbonitrides.

In addition, the sheet spacing of interphase precipitation was directly related to the contribution of precipitation hardening to the yield strength of a microalloyed steel.

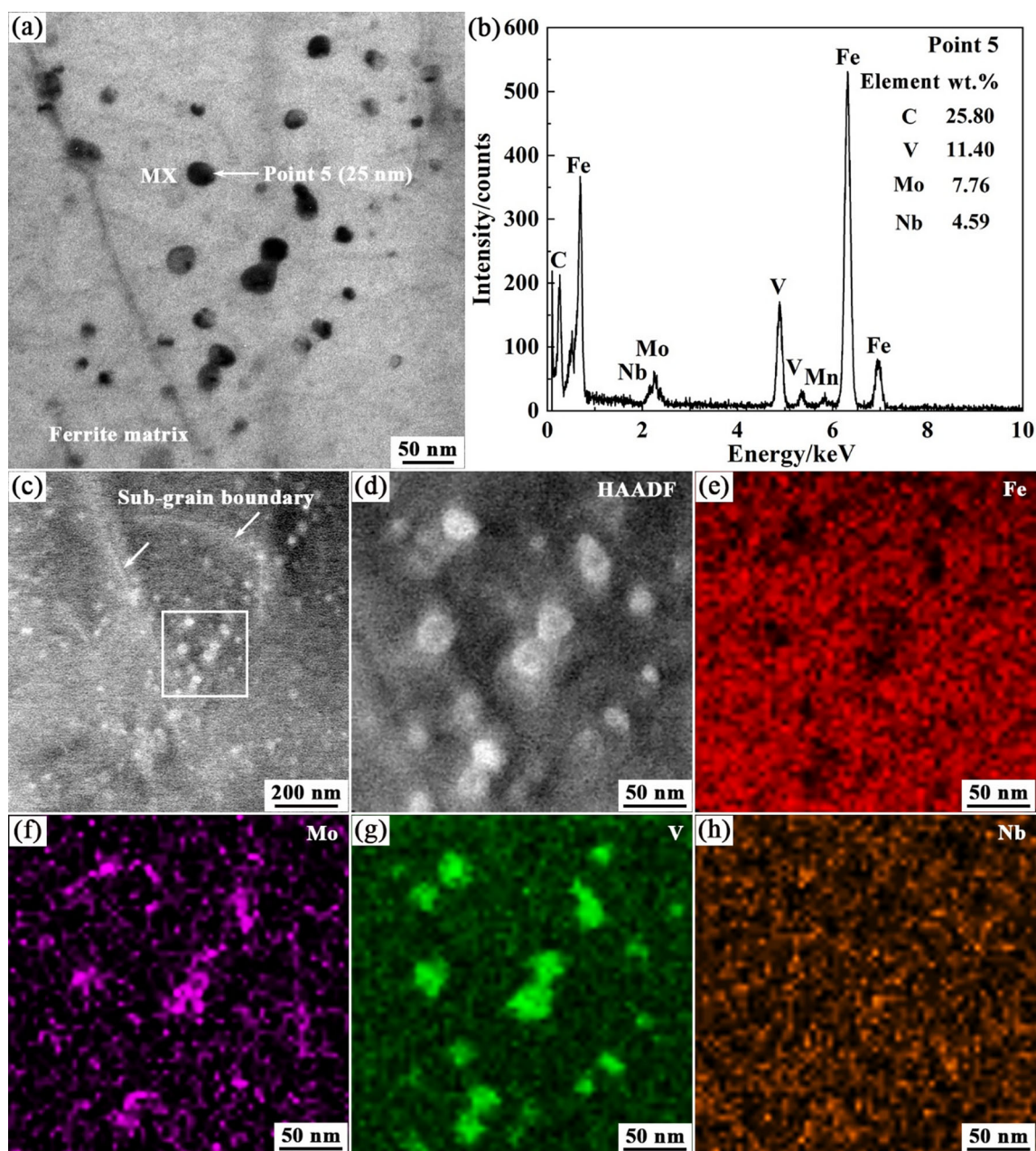


**Fig. 16** TEM analysis of nanosized particles precipitated in 0.26Mo steel cooled at  $0.1\text{ }^{\circ}\text{C s}^{-1}$ . **a** Bright-field image; **b** EDS spectrum; **c** HAADF-STEM micrograph; **d** HAADF-STEM micrograph of

magnified rectangular area in **c**; **e-h** corresponding STEM-EDS maps of precipitates distributed on sub-grain boundaries

Interphase precipitation occurred because of the repeated nucleation of the nanoprecipitates on the migrating  $\gamma/\alpha$  interfaces during the transformation of austenite into ferrite; hence, the sheet spacing largely depended on  $\gamma \rightarrow \alpha$  transformation temperatures of 0Mo, 0.26Mo and 0.50Mo steels, which were directly related to the variations in the amount of Mo in the solid solution. Based on the dynamic CCT curves shown in Fig. 7,  $A_{r3}$  at  $1\text{ }^{\circ}\text{C/s}$  decreased from 749 to 743 and 735  $^{\circ}\text{C}$  when Mo content increased from 0 to 0.26 and 0.50 wt.%, respectively. Evidently, the supercooling

degree ( $\Delta T = A_{e3} - A_{r3}$ ) [8] increased from 71 to 87 and 95  $^{\circ}\text{C}$ , facilitating  $\gamma \rightarrow \alpha$  transformation and increasing the migration rate of  $\gamma/\alpha$  interfaces; thus, the sheet spacing decreased with increasing Mo content, which was consistent with the results obtained by Zhang et al. [12], who reported that low transformation temperatures contributed to decreased sheet spacing. Notably  $\gamma/\alpha$  interfaces migrated so rapidly that the time was probably insufficient for the nucleation and growth of V-rich MX precipitates; thus, it was extremely necessary to consider the intrinsic

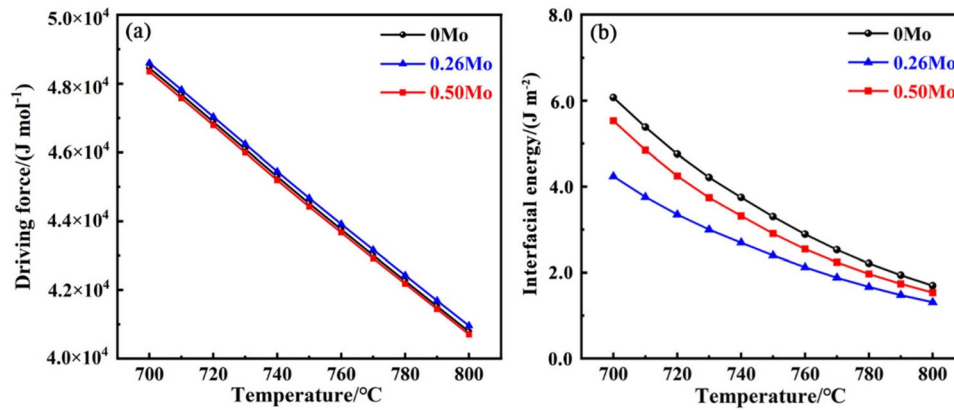


Fig. 17 Precipitation thermodynamics of V-rich MX phase in experimental steels. **a** Driving force; **b** interfacial energy

precipitation thermodynamics of V-rich MX phase to understand the interphase precipitation behavior.

Figure 17 shows that the driving force for the precipitation of V-rich MX phase from the ferrite matrix and the interfacial energy of the precipitates/matrix varied with temperature in ( $\gamma+\alpha$ ) two-phase region. The driving forces corresponding to 0Mo, 0.26Mo and 0.50Mo steels increased from  $4.08 \times 10^4$ ,  $4.10 \times 10^4$  and  $4.07 \times 10^4$  to  $4.85 \times 10^4$ ,  $4.86 \times 10^4$  and  $4.84 \times 10^4$  J/mol, respectively, when the temperature decreased from 800 to 700 °C. Importantly, the driving force for the V-rich MX phase precipitation was enhanced with the sequence of 0.50Mo, 0Mo and 0.26Mo. Moreover, the interfacial energy increased from 1.69, 1.31 and 1.53 to 6.07, 4.24 and 5.53 J/m<sup>2</sup>, respectively, and the resistance to overcome for the precipitation of V-rich MX phase increased in the order of 0.26Mo, 0.50Mo and 0Mo steels.

According to the above-mentioned analysis, a greater driving force accompanied by a lower interfacial energy accelerated interphase precipitation and reduced the sheet spacing by decreasing  $\gamma \rightarrow \alpha$  transformation temperature when Mo content increased from 0 to 0.26 wt.%. By increasing Mo content to 0.50 wt.%, although the further reduced transformation temperature contributed to the decreased sheet spacing, the interphase precipitates were locally distributed in ferrite matrix because of the reduced driving force and increased interfacial energy.

## 5 Conclusions

1. The ferrite microstructure was transformed from polygonal ferrite in 0Mo steel to both acicular ferrite and polygonal ferrite in 0.26Mo and 0.50Mo steels. The maximum area fraction of AF was obtained in 0.26Mo steel.

2. Both thermodynamic calculations and ToF-SIMS analysis and EPMA proved that the solid solution quantity of Mo in austenite obviously increased with increasing Mo content.
3. AF transformation was largely dependent on the solid dissolved Mo, which reduced the austenite decomposition temperature and was further promoted by heterogeneous nucleation on the submicron-scale Nb-rich MX precipitates following the orientation relationship of  $(011)_{MX} // (100)_{\text{Ferrite}}$  and  $[1\bar{1}1]_{MX} // [001]_{\text{Ferrite}}$ .
4. Interphase precipitation of the nanosized V-rich MX particles with Mo partitioning and regular row-like morphologies could be observed, and the sheet spacing evidently decreased as Mo addition increased. Furthermore, the interphase precipitates possessed B–N orientation relationship of  $(100)_{MX} // (100)_{\text{Ferrite}}$  and  $[001]_{MX} // [00\bar{1}]_{\text{Ferrite}}$  with ferrite matrix.

**Acknowledgements** This work is financially supported by the National Natural Science Foundation of China (Grant No. 52104333), the Program for Young Talents of Science and Technology in Universities of Inner Mongolia Autonomous Region (Grant No. NJYT24070), the Natural Science Foundation of Inner Mongolia (Grant No. 2024MS05029) and the Research Project of Carbon Peak and Carbon Neutrality in Universities of Inner Mongolia Autonomous Region (Grant No. STZX202316).

## Declarations

**Conflict of interest** The authors declare no conflict of interest.

## References

- [1] X. Wang, Z. Li, S. Zhou, W. Wang, Q. Yong, Z. Yang, J. Shen, C. Shang, Q. Liu, Mater. Sci. Eng. A 807 (2021) 140865.
- [2] C.T. Gross, D. Isheim, S. Vaynman, M.E. Fine, Y.W. Chung, Metall. Mater. Trans. A 50 (2019) 209–219.

- [3] W. Xiong, R. Song, W. Huo, P. Yu, S. Qin, Z. Liu, *Vacuum* 195 (2022) 110709.
- [4] S.G. Cui, G.C. Gu, C.X. Shi, G.Y. Xiao, Y.P. Lu, *J. Mater. Res. Technol.* 26 (2023) 9190–9202.
- [5] Y. Li, Q. Feng, S. Cui, L. Dai, Q. Liu, S. Jia, H. Zhang, H. Wu, *J. Mater. Res. Technol.* 28 (2024) 2648–2659.
- [6] L.Z. Xu, G.Y. Qiao, X.X. Lu, Y. Gu, K. Xu, X.W. Chen, F.R. Xiao, *Mater. Chem. Phys.* 314 (2024) 128850.
- [7] P. Wang, M. Ryberg, Y. Yang, K. Feng, S. Kara, M. Hauschild, W.Q. Chen, *Nat. Commun.* 12 (2021) 2066.
- [8] S. Xu, R. Cao, J. Gao, Y. Zhang, H. Zhao, S. Wang, Y. Huang, G. Wu, H. Wu, C. Zhang, X. Mao, *Mater. Charact.* 207 (2024) 113504.
- [9] O. Nousiainen, J. Hannula, S. Saukko, A. Kajjalainen, J. Kömi, *Mater. Charact.* 201 (2023) 112944.
- [10] P. Gong, E.J. Palmiere, W.M. Rainforth, *Acta Mater.* 97 (2015) 392–403.
- [11] H. Dong, H. Chen, A. Riyahi Khorasgani, B. Zhang, Y. Zhang, Z. Wang, X. Zhou, W. Wang, H. Wang, T. Li, Z. Yang, S. van der Zwaag, *Acta Mater.* 223 (2022) 117475.
- [12] Y.J. Zhang, G. Miyamoto, K. Shinbo, T. Furuhashi, *Acta Mater.* 186 (2020) 533–544.
- [13] K.F. Rodriguez-Galeano, J. Nutter, Y. Azakli, C. Slater, W.M. Rainforth, *Mater. Sci. Eng. A* 893 (2024) 146140.
- [14] P.P. Singh, S. Mula, S. Ghosh, *Mater. Today Commun.* 38 (2024) 107582.
- [15] Z. Fu, G. Yang, X. Mao, R. Han, Y. Xu, D. Xu, *J. Mater. Res. Technol.* 27 (2023) 8132–8142.
- [16] J. Hu, L.X. Du, J.J. Wang, *Scripta Mater.* 68 (2013) 953–956.
- [17] J.H. Shim, Y.W. Cho, S.H. Chung, J.D. Shim, D.N. Lee, *Acta Mater.* 47 (1999) 2751–2760.
- [18] X. Zhou, D. Wang, J. Tian, T. Qu, Z. Zhang, Y. Wang, X. Li, D. Hou, *Mater. Charact.* 208 (2024) 113659.
- [19] Y. Shao, C. Liu, Z. Yan, H. Li, Y. Liu, *J. Mater. Sci. Technol.* 34 (2018) 737–744.
- [20] T. Yokomizo, M. Enomoto, O. Umezawa, G. Spanos, R.O. Rosenberg, *Mater. Sci. Eng. A* 344 (2003) 261–267.
- [21] S. Wu, C. Zhang, L. Zhu, Q. Zhang, X. Ma, *Scripta Mater.* 185 (2020) 61–65.
- [22] D. Zhang, H. Terasaki, Y.I. Komizo, *Acta Mater.* 58 (2010) 1369–1378.
- [23] M. Díaz-Fuentes, A. Iza-Mendia, I. Gutiérrez, *Metall. Mater. Trans. A* 34 (2003) 2505–2516.
- [24] H. Zhao, J. Gao, G. Wu, H. Wu, C. Zhang, Y. Huang, Y. Luo, X. Yang, S. Wang, *J. Mater. Res. Technol.* 28 (2024) 1957–1966.
- [25] Z. Xiong, S. Liu, X. Wang, C. Shang, X. Li, R.D.K. Misra, *Mater. Sci. Eng. A* 636 (2015) 117–123.
- [26] J. Hu, L.X. Du, M. Zang, S.J. Yin, Y.G. Wang, X.Y. Qi, X.H. Gao, R.D.K. Misra, *Mater. Charact.* 118 (2016) 446–453.
- [27] Y.M. Kim, H. Lee, N.J. Kim, *Mater. Sci. Eng. A* 478 (2008) 361–370.
- [28] S.F. Medina, M. Gómez, L. Rancel, *Scripta Mater.* 58 (2008) 1110–1113.
- [29] J. Zhang, W. Xin, Z. Ge, G. Luo, J. Peng, *Mater. Charact.* 199 (2023) 112849.
- [30] P. Bai, C. Shang, H.H. Wu, G. Ma, S. Wang, G. Wu, J. Gao, Y. Chen, J. Zhang, J. Zhu, X. Mao, *J. Mater. Res. Technol.* 25 (2023) 6949–6964.
- [31] S. Lv, H.H. Wu, K. Wang, S. Wang, G. Wu, J. Gao, X.S. Yang, J. Zhu, X. Mao, *Comput. Mater. Sci.* 218 (2023) 111989.
- [32] J.T. Wang, P.D. Hodgson, I. Bikmukhametov, M.K. Miller, I. Timokhina, *Mater. Des.* 141 (2018) 48–56.
- [33] C. Ledermueller, H.I. Pratiwi, R.F. Webster, M. Eizadjou, S.P. Ringer, S. Primig, *Mater. Des.* 185 (2020) 108278.
- [34] Z. Tang, W. Stumpf, *Mater. Charact.* 59 (2008) 717–728.
- [35] C. García de Andrés, C. Capdevila, I. Madariaga, I. Gutiérrez, *Scripta Mater.* 45 (2001) 709–716.
- [36] J.H. Kong, L. Zhen, B. Guo, P.H. Li, A.H. Wang, C.S. Xie, *Mater. Des.* 25 (2004) 723–728.
- [37] M.C. Zhao, K. Yang, F.R. Xiao, Y.Y. Shan, *Mater. Sci. Eng. A* 355 (2003) 126–136.
- [38] H. Hu, G. Xu, L. Wang, Z. Xue, Y. Zhang, G. Liu, *Mater. Des.* 84 (2015) 95–99.
- [39] L. Shi, Z.S. Yan, Y.C. Liu, X. Yang, C. Zhang, H.J. Li, *Int. J. Miner. Metall. Mater.* 21 (2014) 1167–1174.
- [40] L. Shi, Z.S. Yan, Y.C. Liu, X. Yang, Z.X. Qiao, B.Q. Ning, H.J. Li, *Met. Mater. Int.* 20 (2014) 19–25.
- [41] S.W. Thompson, D.J. Vin Col, G. Krauss, *Metall. Trans. A* 21 (1990) 1493–1507.
- [42] W. Hui, Y. Zhang, C. Shao, S. Chen, X. Zhao, H. Dong, *J. Mater. Sci. Technol.* 32 (2016) 545–551.
- [43] J. Moon, T.H. Lee, S.D. Kim, C.H. Lee, J.H. Jang, J.H. Shin, J. W. Lee, B.H. Lee, D.W. Suh, *Mater. Charact.* 170 (2020) 110677.
- [44] Y. Xu, W. Zhang, M. Sun, H. Yi, Z. Liu, *Mater. Lett.* 139 (2015) 177–181.
- [45] I. Bikmukhametov, H. Beladi, J. Wang, P.D. Hodgson, I. Timokhina, *Acta Mater.* 170 (2019) 75–86.
- [46] N. Singh, G. Casillas, D. Wexler, C. Killmore, E. Pereloma, *Acta Mater.* 201 (2020) 386–402.
- [47] Y. Funakawa, T. Shiozaki, K. Tomita, T. Yamamoto, E. Maeda, *ISIJ Int.* 44 (2004) 1945–1951.
- [48] Y. Funakawa, T. Fujita, K. Yamada, *JFE Technical Report* 18 (2013) 74–79.
- [49] J. Wang, H. Beladi, L. Pan, F. Fang, J. Hu, L. Kong, P.D. Hodgson, I. Timokhina, *Mater. Sci. Eng. A* 804 (2021) 140518.
- [50] L. Jiang, R.K.W. Marceau, T. Dorin, K. Wood, P.D. Hodgson, N. Stanford, *Mater. Charact.* 166 (2020) 110444.
- [51] S. Chen, L. Li, Z. Peng, X. Huo, H. Sun, *J. Mater. Res. Technol.* 10 (2021) 580–593.
- [52] P. Gong, X.G. Liu, A. Rijkenberg, W.M. Rainforth, *Acta Mater.* 161 (2018) 374–387.
- [53] N. Kamikawa, Y. Abe, G. Miyamoto, Y. Funakawa, T. Furuhashi, *ISIJ Int.* 54 (2014) 212–221.
- [54] J.H. Jang, C.H. Lee, Y.U. Heo, D.W. Suh, *Acta Mater.* 60 (2012) 208–217.
- [55] J. Yoo, M.C. Jo, J. Bian, S.S. Sohn, S. Lee, *Mater. Charact.* 176 (2021) 111133.

Springer Nature or its licensor (e.g. a society or other partner) holds exclusive rights to this article under a publishing agreement with the author(s) or other rightsholder(s); author self-archiving of the accepted manuscript version of this article is solely governed by the terms of such publishing agreement and applicable law.